

System size dependence of transverse momentum correlations at $\sqrt{s_{NN}}=62.4$ and 200 GeV at the BNL Relativistic Heavy Ion Collider

L. Adamczyk,¹ J. K. Adkins,²³ G. Agakishiev,²¹ M. M. Aggarwal,³⁴ Z. Ahammed,⁵³ I. Alekseev,¹⁹ J. Alford,²² C. D. Anson,³¹ A. Aparin,²¹ D. Arkhipkin,⁴ E. Aschenauer,⁴ G. S. Averichev,²¹ J. Balewski,²⁶ A. Banerjee,⁵³ Z. Barnovska,¹⁴ D. R. Beavis,⁴ R. Bellwied,⁴⁹ M. J. Betancourt,²⁶ R. R. Betts,¹⁰ A. Bhasin,²⁰ A. K. Bhati,³⁴ Bhattarai,⁴⁸ H. Bichsel,⁵⁵ J. Bielcik,¹³ J. Bielcikova,¹⁴ L. C. Bland,⁴ I. G. Bordyuzhin,¹⁹ W. Borowski,⁴⁵ J. Bouchet,²² A. V. Brandin,²⁹ S. G. Brovko,⁶ E. Bruna,⁵⁷ S. Bültmann,³² I. Bunzarov,²¹ T. P. Burton,⁴ J. Butterworth,⁴⁰ X. Z. Cai,⁴⁴ H. Caines,⁵⁷ M. Calderón de la Barca Sánchez,⁶ D. Cebra,⁶ R. Cendejas,³⁵ M. C. Cervantes,⁴⁷ P. Chaloupka,¹³ Z. Chang,⁴⁷ S. Chattopadhyay,⁵³ H. F. Chen,⁴² J. H. Chen,⁴⁴ J. Y. Chen,⁹ L. Chen,⁹ J. Cheng,⁵⁰ M. Cherney,¹² A. Chikanian,⁵⁷ W. Christie,⁴ P. Chung,¹⁴ J. Chwastowski,¹¹ M. J. M. Coddington,⁴⁸ R. Corliss,²⁶ J. G. Cramer,⁵⁵ H. J. Crawford,⁵ X. Cui,⁴² S. Das,¹⁶ A. Davila Leyva,⁴⁸ L. C. De Silva,⁴⁹ R. R. Debbé,⁴ T. G. Dedovich,²¹ J. Deng,⁴³ R. Derradi de Souza,⁸ S. Dhamija,¹⁸ B. di Ruzza,⁴ L. Didenko,⁴ F. Ding,⁶ A. Dion,⁴ P. Djawotho,⁴⁷ X. Dong,²⁵ J. L. Drachenberg,⁵² J. E. Draper,⁶ C. M. Du,²⁴ L. E. Dunkelberger,⁷ J. C. Dunlop,⁴ L. G. Efimov,²¹ M. Elnimr,⁵⁶ J. Engelage,⁵ G. Eppley,⁴⁰ L. Eun,²⁵ O. Evdokimov,¹⁰ R. Fatemi,²³ S. Fazio,⁴ J. Fedorisin,²¹ R. G. Fersch,²³ P. Filip,²¹ E. Finch,⁵⁷ Y. Fisyak,⁴ E. Flores,⁶ C. A. Gagliardi,⁴⁷ D. R. Gangadharan,³¹ D. Garand,³⁷ F. Geurts,⁴⁰ A. Gibson,⁵² S. Gliske,² O. G. Grebenyuk,²⁵ D. Grosnick,⁵² A. Gupta,²⁰ S. Gupta,²⁰ W. Guryn,⁴ B. Haag,⁶ O. Hajkova,¹³ A. Hamed,⁴⁷ L.-X. Han,⁴⁴ J. W. Harris,⁵⁷ J. P. Hays-Wehle,²⁶ S. Heppelmann,³⁵ A. Hirsch,³⁷ G. W. Hoffmann,⁴⁸ D. J. Hofman,¹⁰ S. Horvat,⁵⁷ B. Huang,⁴ H. Z. Huang,⁷ P. Huck,⁹ T. J. Humanic,³¹ G. Igo,⁷ W. W. Jacobs,¹⁸ C. Jena,³⁰ E. G. Judd,⁵ S. Kabana,⁴⁵ K. Kang,⁵⁰ J. Kapitan,¹⁴ K. Kauder,¹⁰ H. W. Ke,⁹ D. Keane,²² A. Kechechyan,²¹ A. Kesich,⁶ D. P. Kikola,³⁷ J. Kiryluk,²⁵ I. Kisel,²⁵ A. Kisiel,⁵⁴ S. R. Klein,²⁵ D. D. Koetke,⁵² T. Kollegger,¹⁵ J. Konzer,³⁷ I. Koralt,³² W. Korsch,²³ L. Kotchenda,²⁹ P. Kravtsov,²⁹ K. Krueger,² I. Kulakov,²⁵ L. Kumar,²² M. A. C. Lamont,⁴ J. M. Landgraf,⁴ K. D. Landry,⁷ S. LaPointe,⁵⁶ J. Lauret,⁴ A. Lebedev,⁴ R. Lednicky,²¹ J. H. Lee,⁴ W. Leight,²⁶ M. J. LeVine,⁴ C. Li,⁴² W. Li,⁴⁴ X. Li,³⁷ X. Li,⁴⁶ Y. Li,⁵⁰ Z. M. Li,⁹ L. M. Lima,⁴¹ M. A. Lisa,³¹ F. Liu,⁹ T. Ljubicic,⁴ W. J. Llope,⁴⁰ R. S. Longacre,⁴ Y. Lu,⁴² X. Luo,⁹ A. Luszczak,¹¹ G. L. Ma,⁴⁴ Y. G. Ma,⁴⁴ D. M. M. D. Madagodagettige Don,¹² D. P. Mahapatra,¹⁶ R. Majka,⁵⁷ S. Margetis,²² C. Markert,⁴⁸ H. Masui,²⁵ H. S. Matis,²⁵ D. McDonald,⁴⁰ T. S. McShane,¹² S. Mioduszewski,⁴⁷ M. K. Mitrovski,⁴ Y. Mohammed,⁴⁷ B. Mohanty,³⁰ M. M. Mondal,³ M. G. Munhoz,⁴¹ M. K. Mustafa,³⁷ M. Naglis,²⁵ B. K. Nandi,¹⁷ Md. Nasim,⁵³ T. K. Nayak,⁵³ J. M. Nelson,³ L. V. Nogach,³⁶ J. Novak,²⁸ G. Odyniec,²⁵ A. Ogawa,⁴ K. Oh,³⁸ A. Ohlson,⁵⁷ V. Okorokov,²⁹ E. W. Oldag,⁴⁸ R. A. N. Oliveira,⁴¹ D. Olson,²⁵ M. Pachr,¹³ B. S. Page,¹⁸ S. K. Pal,⁵³ Y. X. Pan,⁷ Y. Pandit,¹⁰ Y. Panebratsev,²¹ T. Pawlak,⁵⁴ B. Pawlik,³³ H. Pei,¹⁰ C. Perkins,⁵ W. Peryt,⁵⁴ P. Pile,⁴ M. Planinic,⁵⁸ J. Pluta,⁵⁴ N. Poljak,⁵⁸ J. Porter,²⁵ A. M. Poskanzer,²⁵ C. B. Powell,²⁵ C. Pruneau,⁵⁶ N. K. Pruthi,³⁴ M. Przybycien,¹ P. R. Pujahari,¹⁷ J. Putschke,⁵⁶ H. Qiu,²⁵ S. Ramachandran,²³ R. Raniwala,³⁹ S. Raniwala,³⁹ R. L. Ray,⁴⁸ R. Redwine,²⁶ C. K. Riley,⁵⁷ H. G. Ritter,²⁵ J. B. Roberts,⁴⁰ O. V. Rogachevskiy,²¹ J. L. Romero,⁶ J. F. Ross,¹² L. Ruan,⁴ J. Rusnak,¹⁴ N. R. Sahoo,⁵³ P. K. Sahu,¹⁶ I. Sakrejda,²⁵ S. Salur,²⁵ A. Sandacz,⁵⁴ J. Sandweiss,⁵⁷ E. Sangaline,⁶ A. Sarkar,¹⁷ J. Schambach,⁴⁸ R. P. Scharenberg,³⁷ A. M. Schmah,²⁵ B. Schmidke,⁴ N. Schmitz,²⁷ T. R. Schuster,¹⁵ J. Seele,²⁶ J. Seger,¹² P. Seyboth,²⁷ N. Shah,⁷ E. Shahaliev,²¹ M. Shao,⁴² B. Sharma,³⁴ M. Sharma,⁵⁶ S. S. Shi,⁹ Q. Y. Shou,⁴⁴ E. P. Sichtermann,²⁵ R. N. Singaraju,⁵³ M. J. Skoby,¹⁸ D. Smirnov,⁴ N. Smirnov,⁵⁷ D. Solanki,³⁹ P. Sorensen,⁴ U. G. deSouza,⁴¹ H. M. Spinka,² B. Srivastava,³⁷ T. D. S. Stanislaus,⁵² S. G. Steadman,²⁶ J. R. Stevens,²⁶ R. Stock,¹⁵ M. Strikhanov,²⁹ B. Stringfellow,³⁷ A. A. P. Suaide,⁴¹ M. C. Suarez,¹⁰ M. Sumbera,¹⁴ X. M. Sun,²⁵ Y. Sun,⁴² Z. Sun,²⁴ B. Surrow,⁴⁶ D. N. Svirida,¹⁹ T. J. M. Symons,²⁵ A. Szanto de Toledo,⁴¹ J. Takahashi,⁸ A. H. Tang,⁴ Z. Tang,⁴² L. H. Tarini,⁵⁶ T. Tarnowsky,²⁸ J. H. Thomas,²⁵ J. Tian,⁴⁴ A. R. Timmins,⁴⁹ D. Tlusty,¹⁴ M. Tokarev,²¹ S. Trentalange,⁷ R. E. Tribble,⁴⁷ P. Tribedy,⁵³ B. A. Trzeciak,⁵⁴ O. D. Tsai,⁷ J. Turnau,³³ T. Ullrich,⁴ D. G. Underwood,² G. Van Buren,⁴ G. van Nieuwenhuizen,²⁶ J. A. Vanfossen, Jr.,²² R. Varma,¹⁷ G. M. S. Vasconcelos,⁸ F. Videbæk,⁴ Y. P. Viyogi,⁵³ S. Vokal,²¹ S. A. Voloshin,⁵⁶ A. Vossen,¹⁸ M. Wada,⁴⁸ F. Wang,³⁷ G. Wang,⁷ H. Wang,⁴ J. S. Wang,²⁴ Q. Wang,³⁷ X. L. Wang,⁴² Y. Wang,⁵⁰ G. Webb,²³ J. C. Webb,⁴ G. D. Westfall,²⁸ C. Whitten Jr.,⁷ H. Wieman,²⁵ S. W. Wissink,¹⁸ R. Witt,⁵¹ Y. F. Wu,⁹ Z. Xiao,⁵⁰ W. Xie,³⁷ K. Xin,⁴⁰ H. Xu,²⁴ N. Xu,²⁵ Q. H. Xu,⁴³ W. Xu,⁷ Y. Xu,⁴² Z. Xu,⁴ L. Xue,⁴⁴ Y. Yang,²⁴ Y. Yang,⁹ P. Yepes,⁴⁰ L. Yi,³⁷ K. Yip,⁴ I.-K. Yoo,³⁸ M. Zawisza,⁵⁴ H. Zbroszczyk,⁵⁴ J. B. Zhang,⁹ S. Zhang,⁴⁴ X. P. Zhang,⁵⁰ Y. Zhang,⁴² Z. P. Zhang,⁴² F. Zhao,⁷ J. Zhao,⁴⁴ C. Zhong,⁴⁴ X. Zhu,⁵⁰ Y. H. Zhu,⁴⁴ Y. Zoukarnieva,²¹ and M. Zyzak²⁵

(STAR Collaboration)

- ¹AGH University of Science and Technology, Cracow, Poland
²Argonne National Laboratory, Argonne, Illinois 60439, USA
³University of Birmingham, Birmingham, United Kingdom
⁴Brookhaven National Laboratory, Upton, New York 11973, USA
⁵University of California, Berkeley, California 94720, USA
⁶University of California, Davis, California 95616, USA
⁷University of California, Los Angeles, California 90095, USA
⁸Universidade Estadual de Campinas, Sao Paulo, Brazil
⁹Central China Normal University (HZNU), Wuhan 430079, China
¹⁰University of Illinois at Chicago, Chicago, Illinois 60607, USA
¹¹Cracow University of Technology, Cracow, Poland
¹²Creighton University, Omaha, Nebraska 68178, USA
¹³Czech Technical University in Prague, FNSPE, Prague, 115 19, Czech Republic
¹⁴Nuclear Physics Institute AS CR, 250 68 Řež/Prague, Czech Republic
¹⁵University of Frankfurt, Frankfurt, Germany
¹⁶Institute of Physics, Bhubaneswar 751005, India
¹⁷Indian Institute of Technology, Mumbai, India
¹⁸Indiana University, Bloomington, Indiana 47408, USA
¹⁹Alikhanov Institute for Theoretical and Experimental Physics, Moscow, Russia
²⁰University of Jammu, Jammu 180001, India
²¹Joint Institute for Nuclear Research, Dubna, 141 980, Russia
²²Kent State University, Kent, Ohio 44242, USA
²³University of Kentucky, Lexington, Kentucky, 40506-0055, USA
²⁴Institute of Modern Physics, Lanzhou, China
²⁵Lawrence Berkeley National Laboratory, Berkeley, California 94720, USA
²⁶Massachusetts Institute of Technology, Cambridge, MA 02139-4307, USA
²⁷Max-Planck-Institut für Physik, Munich, Germany
²⁸Michigan State University, East Lansing, Michigan 48824, USA
²⁹Moscow Engineering Physics Institute, Moscow Russia
³⁰National Institute of Science Education and Research, Bhubaneswar 751005, India
³¹Ohio State University, Columbus, Ohio 43210, USA
³²Old Dominion University, Norfolk, VA, 23529, USA
³³Institute of Nuclear Physics PAN, Cracow, Poland
³⁴Panjab University, Chandigarh 160014, India
³⁵Pennsylvania State University, University Park, Pennsylvania 16802, USA
³⁶Institute of High Energy Physics, Protvino, Russia
³⁷Purdue University, West Lafayette, Indiana 47907, USA
³⁸Pusan National University, Pusan, Republic of Korea
³⁹University of Rajasthan, Jaipur 302004, India
⁴⁰Rice University, Houston, Texas 77251, USA
⁴¹Universidade de Sao Paulo, Sao Paulo, Brazil
⁴²University of Science & Technology of China, Hefei 230026, China
⁴³Shandong University, Jinan, Shandong 250100, China
⁴⁴Shanghai Institute of Applied Physics, Shanghai 201800, China
⁴⁵SUBATECH, Nantes, France
⁴⁶Temple University, Philadelphia, Pennsylvania, 19122
⁴⁷Texas A&M University, College Station, Texas 77843, USA
⁴⁸University of Texas, Austin, Texas 78712, USA
⁴⁹University of Houston, Houston, TX, 77204, USA
⁵⁰Tsinghua University, Beijing 100084, China
⁵¹United States Naval Academy, Annapolis, MD 21402, USA
⁵²Valparaiso University, Valparaiso, Indiana 46383, USA
⁵³Variable Energy Cyclotron Centre, Kolkata 700064, India
⁵⁴Warsaw University of Technology, Warsaw, Poland
⁵⁵University of Washington, Seattle, Washington 98195, USA
⁵⁶Wayne State University, Detroit, Michigan 48201, USA
⁵⁷Yale University, New Haven, Connecticut 06520, USA
⁵⁸University of Zagreb, Zagreb, HR-10002, Croatia

We present a study of the average transverse momentum (p_t) fluctuations and p_t correlations for charged particles produced in Cu+Cu collisions at midrapidity for $\sqrt{s_{NN}} = 62.4$ and 200 GeV. These results are compared with those published for Au+Au collisions at the same energies, to explore the system size dependence. In addition to the collision energy and system size dependence, the p_t correlation results have been studied as functions of the collision centralities, the ranges in p_t ,

the pseudorapidity η , and the azimuthal angle ϕ . The square root of the measured p_t correlations when scaled by mean p_t is found to be independent of both colliding beam energy and system size studied. Transport-based model calculations are found to have a better quantitative agreement with the measurements compared to models which incorporate only jetlike correlations.

PACS numbers: 25.75.Gz

I. INTRODUCTION

The study of event-by-event fluctuations and correlations is an important tool to understand thermalization and phase transitions in heavy-ion collisions [1–6]. Non-monotonic change in transverse momentum (p_t) correlations as a function of centrality and/or the incident energy has been proposed as a possible signal of quark gluon plasma (QGP) formation [1]. The QGP is believed to be formed at the early stage of high energy heavy-ion collisions when the system is hot and dense. As time passes, the system dilutes, cools down and hadronizes. Fluctuations are supposed to be sensitive to the dynamics of the system, especially at the QGP to hadron gas transition [4, 6]. Alternatively, analyses at the Relativistic Heavy Ion Collider (RHIC) based on p_t auto-correlations (the inversion of the mean transverse momentum fluctuations in various pseudorapidity and azimuthal angle difference regions of the produced particles) indicate that the basic correlation mechanism could be dominated by the process of parton fragmentation [7]. Thus fluctuation measurements are proposed to be an important tool in understanding nucleus-nucleus collisions [1, 5, 6, 8–12]. In addition, under the assumption that thermodynamics is applicable to heavy-ion collisions, fluctuations in various observables could be related to thermodynamic properties of the matter formed. For example, the event-by-event $\langle p_t \rangle$ could be related to temperature fluctuations [13–17].

The study of event-by-event fluctuations of various quantities such as eventwise mean transverse momentum ($\langle p_t \rangle$), charged track multiplicity, and conserved quantities such as net-baryon and/or net-charge number are considered to be some of the main probes in the search for the critical point in the QCD phase diagram [17–26]. One expects enhanced fluctuations in the above observables when the system passes through the vicinity of the critical point. Recent results from the CERN Super Proton Synchrotron (SPS) experiments show that the energy dependence of transverse momentum fluctuations does not show the increase expected for freeze-out near the critical point of QCD [27]. However, when these fluctuations are studied as a function of the system size (colliding C+C, Si+Si, Pb+Pb), enhanced fluctuations are observed in smaller colliding systems [28]. The results from the RHIC beam energy scan (BES) [29] data for the above observables will provide further insights.

The results presented here are from Cu+Cu collisions at $\sqrt{s_{NN}} = 62.4$ and 200 GeV using the solenoidal tracker At RHIC (STAR) and are compared with the published results from Au+Au collisions at the same energies [30].

This paper describes a systematic study of the system size dependence of the transverse momentum correlations observed at RHIC.

The paper is organized as follows. The STAR detector, the data set, and the centrality selection used in the analysis, are discussed in Sec. II. In Sec. III, we discuss $\langle p_t \rangle$ fluctuations extracted from the $\langle p_t \rangle$ distributions, which are compared with mixed events and gamma distributions. Dynamical fluctuations are extracted and presented for Au+Au and Cu+Cu collisions at $\sqrt{s_{NN}} = 62.4$ and 200 GeV. The p_t correlations and the dynamical correlations when scaled by $\langle N_{\text{part}} \rangle$ and $\langle p_t \rangle$ are discussed in Sec. IV, to understand the centrality and energy dependence. Experimental data is also compared to various model calculations. Finally, a detailed study of η , ϕ and p_t dependence of the correlations, is presented. The systematic errors associated with the analysis are discussed in Sec. V. We conclude with a summary in Sec. VI.

II. EXPERIMENT AND DATA ANALYSIS

The Cu+Cu data were taken using the STAR detector with a minimum bias trigger. For the data taken at $\sqrt{s_{NN}} = 200$ GeV this was done by requiring a coincidence from the two zero degree calorimeters (ZDCs). For the $\sqrt{s_{NN}} = 62.4$ GeV data, the ZDC is less efficient, so a beam beam counter (BBC) coincidence was also required. More details about the trigger detectors can be obtained from Ref. [31].

The main detector used in this analysis is the time projection chamber (TPC) [32], which is the primary tracking device in STAR. The TPC is 4.2 m long and 4 m in diameter and its acceptance spans about ± 1.0 units of pseudorapidity and full azimuthal coverage. The sensitive volume of the TPC contains P10 gas (10% methane, 90% argon) regulated at 2 mbar above atmospheric pressure. The TPC data are used to determine particle trajectories, momenta, and particle-type through ionization energy loss (dE/dx) [33].

The primary vertex of events used in this analysis is required to be within ± 30 cm of the geometric center of the TPC along the beam axis. This selection process provides about 7.5×10^6 and 15×10^6 minimum bias events for Cu+Cu collisions at $\sqrt{s_{NN}} = 62.4$ and 200 GeV, respectively.

The collision centralities are represented by the fractions of events in the minimum bias inelastic cross section distribution in a collision. In data, the collision centrality is determined by using the uncorrected charged track multiplicity ($N_{\text{ch}}^{\text{TPC}}$), measured in the TPC within

$|\eta| < 0.5$. The various centrality bins are calculated as a fraction of this multiplicity distribution starting at the highest multiplicities. The centrality classes for Cu+Cu collisions at $\sqrt{s_{NN}} = 62.4$ and 200 GeV are 0%–10% (most central), 10%–20%, 20%–30%, 30%–40%, 40%–50% and 50%–60% (most peripheral). Each centrality bin is associated with an average number of participating nucleons ($\langle N_{\text{part}} \rangle$) obtained using Glauber Monte Carlo simulations [34] employing the Woods-Saxon distribution for the nucleons inside the Cu nucleus. The systematic uncertainties include those determined by varying the Woods-Saxon parameters, those associated with the nucleon-nucleon cross sections, those related to the functional representation of the multiplicity distribution, and those associated with the determination of the total Cu+Cu cross section. Table I lists the $N_{\text{ch}}^{\text{TPC}}$ and $\langle N_{\text{part}} \rangle$ values for each centrality in Cu+Cu collisions at $\sqrt{s_{NN}} = 62.4$ and 200 GeV. Corresponding values for Au+Au collisions can be found in Ref. [34].

In order to have uniform detector performance, a pseudorapidity cut of $|\eta| < 1.0$ is applied to tracks. To avoid the admixture of tracks from a secondary vertex, a requirement is placed on the distance of closest approach (DCA) between each track and the event vertex. The charged particle tracks are required to have originated within 1 cm of the measured event vertex. The multiple counting of split tracks (more than one track reconstructed from the original single track) is avoided by applying a condition on the number of track fit points (N_{Fit}) used in the reconstruction of the track. Each included track is required to have a minimum number of 21 TPC points along the track. The transverse momentum range selected for the analysis is 0.15–2.0 GeV/ c .

The errors shown in the figures have the statistical and systematic errors added in quadrature unless otherwise stated. The statistical errors are small and are within symbol sizes. The final systematic errors are obtained as quadrature sums of systematic errors from different sources as discussed in Sec. V.

III. $\langle p_t \rangle$ FLUCTUATIONS

The p_t fluctuations in high energy collisions can be measured using the distribution of the event-wise mean transverse momentum defined as

$$\langle p_t \rangle = \frac{1}{N} \sum_{i=1}^N p_{t,i}, \quad (1)$$

where N is the multiplicity of accepted tracks from the primary vertex in a given event and $p_{t,i}$ is the transverse momentum of the i th track. The mean- p_t distribution is compared to the corresponding distribution obtained for mixed events [30]. Mixed events are constructed by randomly selecting one track from an event chosen from the events in the same centrality and same event vertex bin. The mixed events are created with the same multiplicity distribution as that of the real events.

TABLE I: The $N_{\text{ch}}^{\text{TPC}}$ values and average number of participating nucleons ($\langle N_{\text{part}} \rangle$) for various collision centralities in Cu+Cu collisions at $\sqrt{s_{NN}} = 62.4$ and 200 GeV.

| % cross section | Cu+Cu 62.4 GeV | | Cu+Cu 200 GeV | |
|-----------------|------------------------------|-----------------------------------|------------------------------|-----------------------------------|
| | $N_{\text{ch}}^{\text{TPC}}$ | $\langle N_{\text{part}} \rangle$ | $N_{\text{ch}}^{\text{TPC}}$ | $\langle N_{\text{part}} \rangle$ |
| 0-10 | > 101 | $96.4^{+1.1}_{-2.6}$ | > 139 | $99.0^{+1.5}_{-1.2}$ |
| 10-20 | 71 – 100 | $72.2^{+0.6}_{-1.9}$ | 98 – 138 | $74.6^{+1.3}_{-1.0}$ |
| 20-30 | 49 – 70 | $51.8^{+0.5}_{-1.2}$ | 67 – 97 | $53.7^{+1.0}_{-0.7}$ |
| 30-40 | 33 – 48 | $36.2^{+0.4}_{-0.8}$ | 46 – 66 | $37.8^{+0.7}_{-0.5}$ |
| 40-50 | 22 – 32 | $24.9^{+0.4}_{-0.6}$ | 30 – 45 | $26.2^{+0.5}_{-0.4}$ |
| 50-60 | 14 – 21 | $16.3^{+0.4}_{-0.3}$ | 19 – 29 | $17.2^{+0.4}_{-0.2}$ |

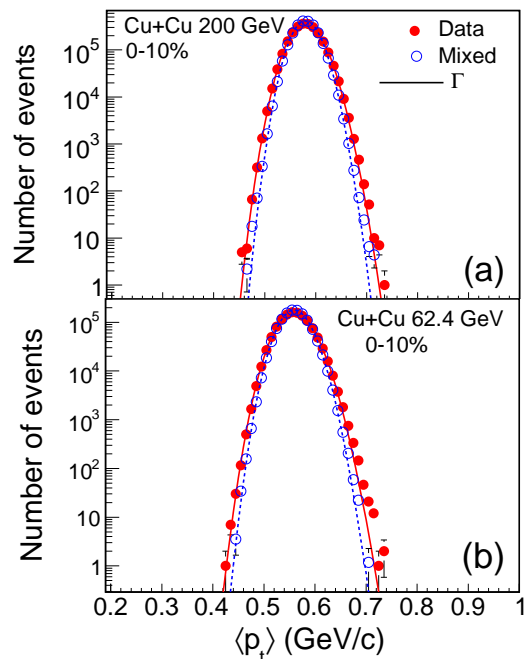


FIG. 1: (Color online) Event-by-event $\langle p_t \rangle$ distributions for data and mixed events in central Cu+Cu collisions at (a) $\sqrt{s_{NN}} = 200$ and (b) 62.4 GeV. The curves (solid for data and dotted for mixed events) represent the Γ distributions. The errors shown are statistical.

Figure 1 shows the event-by-event mean- p_t distributions for 0%–10% Cu+Cu collisions at (a) $\sqrt{s_{NN}} = 200$ and (b) 62.4 GeV. The solid symbols represent the $\langle p_t \rangle$ distributions for data; the open symbols represent $\langle p_t \rangle$ distributions for mixed events. The distributions are similar for other centralities. The mixed events provide a reference measure of statistical fluctuations in the data. Any fluctuations observed in data beyond these

TABLE II: Gamma distribution parameters for event-by-event $\langle p_t \rangle$ distributions for data and mixed events in central (0%-10%) Cu+Cu collisions at $\sqrt{s_{NN}} = 62.4$ and 200 GeV.

| Collision type (AA) | α | β ($\times 10^{-3}$ GeV/c) | μ (GeV/c) | σ (GeV/c) |
|---------------------|----------|-----------------------------------|---------------|------------------|
| Cu 200 (data) | 476 | 1.22 | 0.5805 | 0.02660 |
| Cu 200 (mixed) | 634 | 0.92 | 0.5807 | 0.02310 |
| Cu 62.4 (data) | 358 | 1.56 | 0.5603 | 0.02960 |
| Cu 62.4 (mixed) | 457 | 1.23 | 0.5602 | 0.02621 |

statistical fluctuations are referred to as non-statistical or dynamical fluctuations in this paper. For both data and mixed events, while going from central to peripheral collisions, the mean (μ) of the distributions decreases whereas the standard deviation (σ) increases. Moreover, it is seen that the $\langle p_t \rangle$ distributions for data are wider than those for mixed events, suggesting the presence of non-statistical fluctuations in Cu+Cu data for both 62.4 and 200 GeV collisions.

The curves in Fig. 1 represent the gamma (Γ) distributions for data (solid lines) and mixed events (dotted lines). The Γ distribution [4, 35] is given by

$$f(x) = \frac{x^{\alpha-1} e^{-x/\beta}}{\Gamma(\alpha)\beta^\alpha}, \quad (2)$$

where x represents the $\langle p_t \rangle$; $\alpha = \mu^2/\sigma^2$ and $\beta = \sigma^2/\mu$.

Tannenbaum [35] argues that the Γ distribution is one of the standard representations of the inclusive single particle p_t distribution. Tannenbaum [35] also suggests that the quantity $\alpha/\langle N_{ch} \rangle$, should be ~ 2 , and the quantity $\beta \times \langle N_{ch} \rangle$ representing the inverse slope parameter may be referred to as the temperature of the system. Here $\langle N_{ch} \rangle$ is the average charged particle multiplicity in a given centrality bin. It is found that $\alpha/\langle N_{ch} \rangle$ for Cu+Cu 0%-10% central collisions is 2.04 at 200 GeV, and is 2.18 at 62.4 GeV. The respective $\beta \times \langle N_{ch} \rangle$ values are 0.284 GeV/c and 0.256 GeV/c. The $\alpha/\langle N_{ch} \rangle$ and $\beta \times \langle N_{ch} \rangle$ for 0%-5% central Au+Au collisions at 200 GeV were found to be 1.93 and 0.299 GeV/c [30]. Table II lists gamma distribution parameters for event-by-event $\langle p_t \rangle$ distributions for data and mixed events in central (0%-10%) Cu+Cu collisions at $\sqrt{s_{NN}} = 62.4$ and 200 GeV. The values for Au+Au collisions can be found in Ref. [30]. For Cu+Cu collisions at 200 GeV, $\alpha/\langle N_{ch} \rangle$ varies from 2.04 to 2.11 from central to peripheral collisions. However, for Cu+Cu at 62.4 GeV, $\alpha/\langle N_{ch} \rangle$ varies from 2.18 to 2.27 from central to peripheral collisions. The errors on values of α and β are of the order of 13-18% and 9-12%, respectively, for Cu+Cu collisions.

The non-statistical or dynamical fluctuations in mean- p_t are quantified using a variable σ_{dyn} [36, 37] defined as

$$\sigma_{\text{dyn}} = \sqrt{\left(\frac{\sigma_{\text{data}}}{\mu_{\text{data}}}\right)^2 - \left(\frac{\sigma_{\text{mix}}}{\mu_{\text{mix}}}\right)^2}, \quad (3)$$

where μ_{data} and μ_{mix} are the means of the event-by-event $\langle p_t \rangle$ distributions for data and mixed events, respectively. Similarly, σ_{data} and σ_{mix} are respectively the standard deviations of $\langle p_t \rangle$ distributions for data and mixed events. Figure 2 shows the dynamical fluctuations (σ_{dyn}) in mean- p_t plotted as a function of $\langle N_{\text{part}} \rangle$. The results are shown for Cu+Cu collisions at $\sqrt{s_{NN}} = 62.4$ and 200 GeV, and are compared with the results from Au+Au collisions at $\sqrt{s_{NN}} = 62.4$ and 200 GeV. The dynamical $\langle p_t \rangle$ fluctuations are similar in Au+Au and Cu+Cu collisions at similar values of $\langle N_{\text{part}} \rangle$. The fluctuations decrease as $\langle N_{\text{part}} \rangle$ increases. The dynamical fluctuations are also independent of the collision energy and are found to vary from $\sim 2\%$ to $\sim 5\%$ for $\langle N_{\text{part}} \rangle$ less than ~ 120 . For $\langle N_{\text{part}} \rangle$ greater than ~ 150 , the dynamical fluctuations are smaller and vary from 1% to 2.5%.

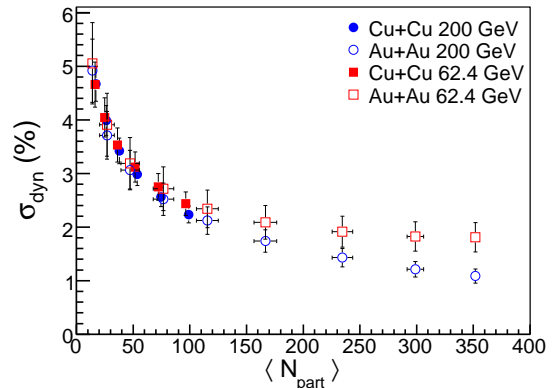


FIG. 2: (Color online) Comparison of dynamical $\langle p_t \rangle$ fluctuations in Au+Au and Cu+Cu collisions at $\sqrt{s_{NN}} = 62.4$ and 200 GeV as a function of the number of participating nucleons.

IV. p_t CORRELATIONS

Non-statistical or dynamical fluctuations can also be analyzed by using two-particle transverse momentum correlations [30]. The two-particle p_t correlations are studied using the following equation [30]:

$$\langle \Delta p_{t,i} \Delta p_{t,j} \rangle = \frac{1}{N_{\text{event}}} \sum_{k=1}^{N_{\text{event}}} \frac{C_k}{N_k(N_k - 1)}, \quad (4)$$

where C_k is the two-particle transverse momentum covariance for the k th event,

$$C_k = \sum_{i=1}^{N_k} \sum_{j=1, i \neq j}^{N_k} (p_{t,i} - \langle p_t \rangle)(p_{t,j} - \langle p_t \rangle), \quad (5)$$

where $p_{t,i}$ is the transverse momentum of the i th track in the k th event, N_k is the number of tracks in the k th

event, and N_{event} is the number of events. The overall event average transverse momentum ($\langle\langle p_t \rangle\rangle$) is given by

$$\langle\langle p_t \rangle\rangle = \left(\sum_{k=1}^{N_{\text{event}}} \langle p_t \rangle_k \right) / N_{\text{event}}, \quad (6)$$

where $\langle p_t \rangle_k$ is the average transverse momentum in the k th event. It may be noted that, for mixed events, there will be no dynamical fluctuations and the p_t correlations will be zero. Equation (4) is used to obtain the p_t correlations in Cu+Cu collisions at $\sqrt{s_{NN}} = 62.4$ and 200 GeV. These results are compared with the published results from Au+Au collisions at similar energies [30] to investigate the system-size and collision energy dependence of the p_t correlations in heavy-ion collisions at RHIC.

The p_t correlation values may be influenced by the dependence of the correlations on the size of the centrality bin due to variation of $\langle\langle p_t \rangle\rangle$ with centrality. This dependence is removed by calculating $\langle\langle p_t \rangle\rangle$ as a function of $\langle N_{\text{ch}} \rangle$, which is the multiplicity of charged tracks used to define the centrality. This multiplicity dependence of $\langle\langle p_t \rangle\rangle$ is fitted with a suitable polynomial in $\langle N_{\text{ch}} \rangle$ and used in Eq. (5) for $\langle\langle p_t \rangle\rangle$. All results presented in this paper have been corrected for this effect.

Figure 3 (a) shows the p_t correlations plotted as a function of $\langle N_{\text{part}} \rangle$ for Cu+Cu and Au+Au collisions at $\sqrt{s_{NN}} = 62.4$ and 200 GeV. The p_t correlations decrease with increasing $\langle N_{\text{part}} \rangle$ for Au+Au and Cu+Cu at both energies. The decrease in correlations with increasing participating nucleons could suggest that correlations are dominated by pairs of particles that originate from the same nucleon-nucleon collision, and they get diluted when the number of participating nucleons increases [30].

A. Scaled p_t Correlations

The decrease in p_t correlations with increasing $\langle N_{\text{part}} \rangle$ seen in Fig. 3 (a) may be related to a system volume dependence characterized by $\langle N_{\text{part}} \rangle$. This volume dependence is removed by multiplying the p_t correlations by $\langle N_{\text{part}} \rangle / 2$ as shown in Fig. 3 (b). The results are shown for Cu+Cu and Au+Au collisions at $\sqrt{s_{NN}} = 62.4$ and 200 GeV. It is observed that this measure of p_t correlations increases quickly with increasing $\langle N_{\text{part}} \rangle$ for both Cu+Cu and Au+Au collisions and saturates for central Au+Au collisions. The saturation of this quantity might indicate effects such as the onset of thermalization [26], the onset of jet quenching [3, 11], or the saturation of transverse flow in central collisions [38]. It seems that, for Cu+Cu collisions, this quantity is larger than for Au+Au collisions which might indicate more correlations for the smaller systems. However, the size of the errors in the current analysis does not allow a conclusive statement.

The correlation measure $\langle \Delta p_{t,i} \Delta p_{t,j} \rangle$ may change due to changes in $\langle\langle p_t \rangle\rangle$ with incident energy and/or collision centrality. To address these changes, the square roots of the measured correlations are scaled

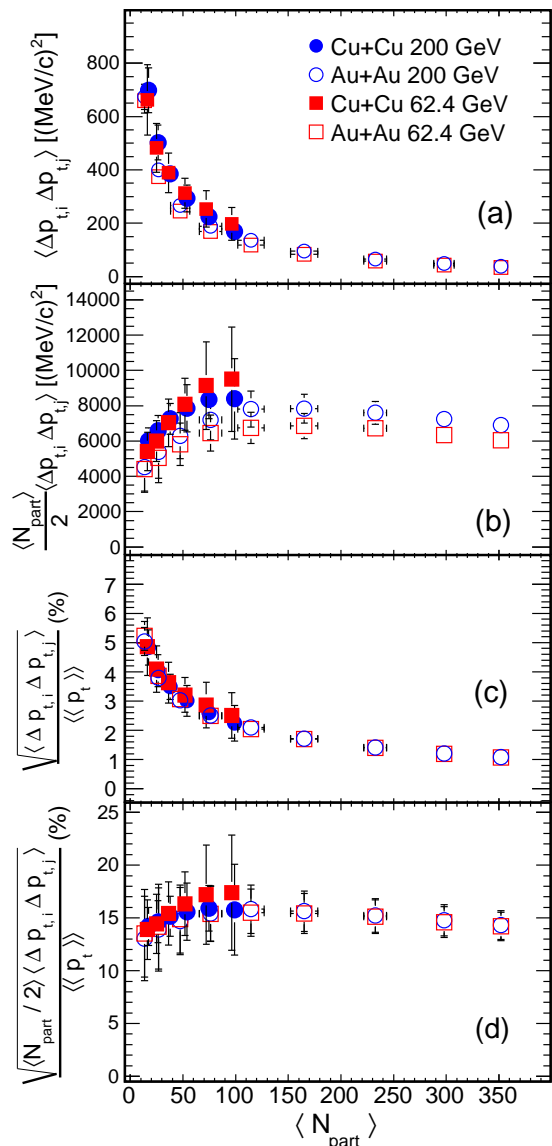


FIG. 3: (Color online) (a) p_t correlations, (b) p_t correlations multiplied by $\langle N_{\text{part}} \rangle / 2$, (c) square root of p_t correlations scaled by $\langle\langle p_t \rangle\rangle$, and (d) square root of p_t correlations multiplied by $\langle N_{\text{part}} \rangle / 2$ and scaled by $\langle\langle p_t \rangle\rangle$, plotted vs. $\langle N_{\text{part}} \rangle$. Results are compared between Cu+Cu and Au+Au collisions at $\sqrt{s_{NN}} = 62.4$ and 200 GeV. Au+Au data have been taken from Ref. [30].

by $\langle\langle p_t \rangle\rangle$. Figure 3 (c) shows the corresponding quantity $\sqrt{\langle \Delta p_{t,i} \Delta p_{t,j} \rangle} / \langle\langle p_t \rangle\rangle$ plotted as a function of collision centrality for Cu+Cu and Au+Au collisions at $\sqrt{s_{NN}} = 62.4$ and 200 GeV. It is observed that the correlation scaled by $\langle\langle p_t \rangle\rangle$ is independent of collision system size and energy, but decreases with increasing $\langle N_{\text{part}} \rangle$. The combined effect of multiplying p_t correlations by $\langle N_{\text{part}} \rangle / 2$ and scaling with $\langle\langle p_t \rangle\rangle$ is shown in Fig. 3 (d). It seems that this quantity $\sqrt{\langle N_{\text{part}} \rangle / 2 \langle \Delta p_{t,i} \Delta p_{t,j} \rangle} / \langle\langle p_t \rangle\rangle$

increases with $\langle N_{\text{part}} \rangle$ and shows saturation for central Au+Au collisions, but is independent of collision system and energy.

B. Model Comparisons

It is interesting to compare the above results with theoretical model calculations to understand the physical mechanism behind these measurements. The comparison is made with some widely used models in heavy-ion collisions such as ultrarelativistic quantum molecular dynamics (URQMD) [39], a multiphase transport model (AMPT) (default and string-melting) [40], and the heavy-ion jet interaction generator (HIJING) (with jet quenching switched off and on) [41]. The model results are obtained using UrQMD version 2.3, AMPT version 1.11 for default, and version 2.11 for AMPT string-melting.

HIJING is a perturbative QCD-inspired model that produces multiple minijet partons; these later get transformed into string configurations and then fragment to hadrons. The fragmentation is based on the Lund jet fragmentation model [42]. A parametrized parton-distribution function inside a nucleus is used to take into account parton shadowing.

AMPT uses the same initial conditions as in HIJING. However, the minijet partons are made to undergo scattering before they are allowed to fragment into hadrons. The string-melting (SM) version of the AMPT model (labeled here as AMPT Melting) is based on the idea that for energy densities beyond a critical value of $1 \text{ GeV}/\text{fm}^3$, the system should be de-confined and strings (or hadrons) decomposed into their partonic components. This is done by converting the mesons to a quark-antiquark pair, baryons to three quarks, and so on. The scattering of the quarks is based on a parton cascade. Once the interactions stop, the partons then hadronize through the mechanism of parton coalescence. The URQMD model is based on a microscopic transport theory where the phase-space description of the reactions is important. It allows for the propagation of all hadrons on classical trajectories in combination with stochastic binary scattering, color string formation, and resonance decay.

Figure 4 shows the comparison of p_t correlations between data [(a) and (c) for Au+Au 200 GeV, and (b) and (d) for Cu+Cu 200 GeV] and the models described above. The transport-based URQMD model calculations are observed to have a better quantitative agreement with the measurements compared to models which incorporate only jetlike correlations as in HIJING. HIJING gives similar dependence on $\langle N_{\text{part}} \rangle$ but under-predicts the magnitude. Inclusion of the jet-quenching effect in HIJING leads to a smaller value of the correlations in central collisions. AMPT model calculation incorporating coalescence as a mechanism of particle production also compares well with data for central collisions. However the default version of this model which incorporates

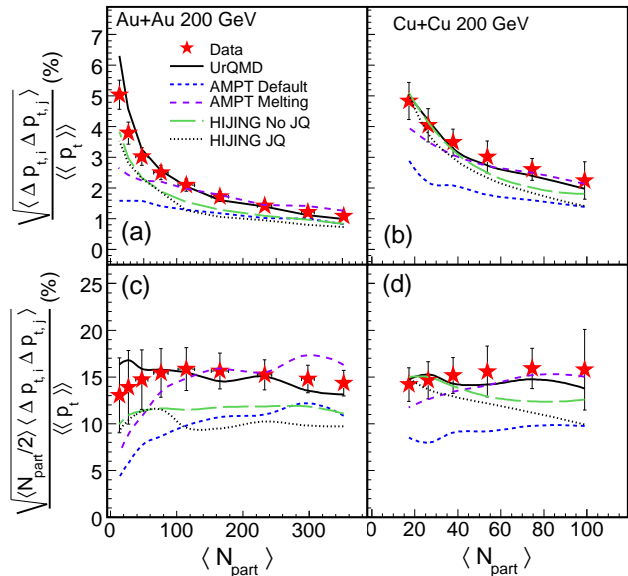


FIG. 4: (Color online) Comparison of scaled p_t correlations between data and models for Au+Au [panels (a) and (c)] and Cu+Cu [panels (b) and (d)] collisions at 200 GeV. Au+Au data has been taken from Ref. [30]. The curves represent different model calculations.

additional initial and final state scattering relative to HIJING yields smaller values of correlations.

C. η and ϕ Dependence

The η and ϕ dependences of p_t correlations are also studied. Figure 5 shows the p_t correlations plotted as a function of increasing rapidity acceptance for Cu+Cu collisions at (a) $\sqrt{s_{NN}} = 200$ and (b) 62.4 GeV. The data points for centralities 0%-10%, 20%-30%, and 40%-50% are shifted by 0.01 in $\Delta\eta/2$ for clarity. The correlations are almost independent of the $\Delta\eta$ window for the most central collisions. For peripheral collisions, the correlations show a slight rapidity dependence with maximum value for $-0.25 < \eta < 0.25$.

Figure 6 shows the p_t correlations for varying azimuthal angle windows for Cu+Cu collisions at (a) $\sqrt{s_{NN}} = 200$ and (b) 62.4 GeV. The data points for $\Delta\phi$ windows: 30° and 90° are shifted by 0.5 units in $\langle N_{\text{part}} \rangle$ for clarity. The p_t correlations are maximum for $\Delta\phi = 15^\circ$ (among the cases studied) and decrease with increasing $\langle N_{\text{part}} \rangle$ for a given $\Delta\phi$ window, as expected. The p_t correlations multiplied by $\langle N_{\text{part}} \rangle/2$ [Fig. 6 (c) for Cu+Cu 200 GeV and Fig. 6 (d) for Cu+Cu 62.4 GeV] seem to increase and then saturate with increasing $\langle N_{\text{part}} \rangle$.

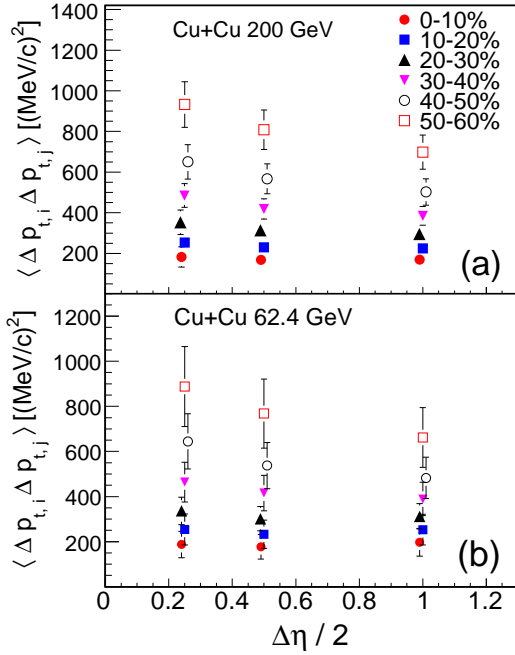


FIG. 5: (Color online) p_t correlations for varying rapidity acceptance ($|\eta| < 0.25, 0.5, \text{ and } 1.0$) for Cu+Cu collisions at $\sqrt{s_{NN}} = 200$ GeV [panel (a)] and 62.4 GeV [panel (b)].

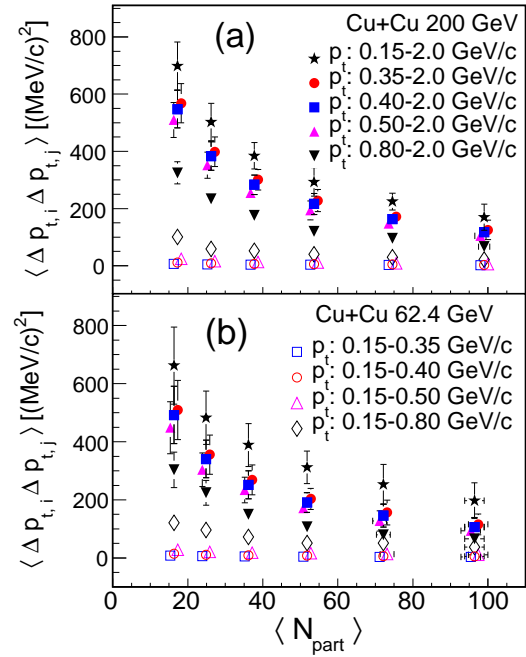


FIG. 7: (Color online) p_t correlations plotted as a function of $\langle N_{\text{part}} \rangle$ for different p_t ranges in Cu+Cu collisions at (a) 200 GeV and (b) 62.4 GeV.

D. p_t Dependence

Figure 7 shows the correlations as a function of collision centrality for different p_t regions in Cu+Cu collisions at (a) $\sqrt{s_{NN}} = 200$ and (b) 62.4 GeV. The different p_t ranges used are shown. These p_t ranges are chosen to demonstrate the dependence of the correlations among tracks sets at lower p_t , at higher p_t , and in a set where all available p_t values are included. The data points for p_t ranges (in GeV/c): 0.15-0.5, 0.5-2.0, 0.15-0.35, and 0.35-2.0, are shifted by one unit in $\langle N_{\text{part}} \rangle$.

The p_t correlation is maximum (minimum) for charged particles whose p_t is in 0.15–2.0 GeV/c (0.15–0.35 GeV/c). The p_t correlation values are small and fairly independent of p_t if a lower p_t bound for the particles studied is fixed at 0.15 GeV/c and the upper p_t bound is progressively increased up to 0.50 GeV/c. When the analysis is carried out by keeping the higher p_t bound fixed at 2.0 GeV/c and subsequently decreasing the lower p_t bound to 0.15 GeV/c, the correlation values are found to increase.

Figure 8 shows the variation of p_t correlations as a function of $\langle N_{\text{part}} \rangle$ for different p_t windows as calculated using the (a) AMPT (string-melting), (b) URQMD, and (c) HIJING (no jet quenching) model calculations for Cu+Cu collisions at 200 GeV. The AMPT calculations

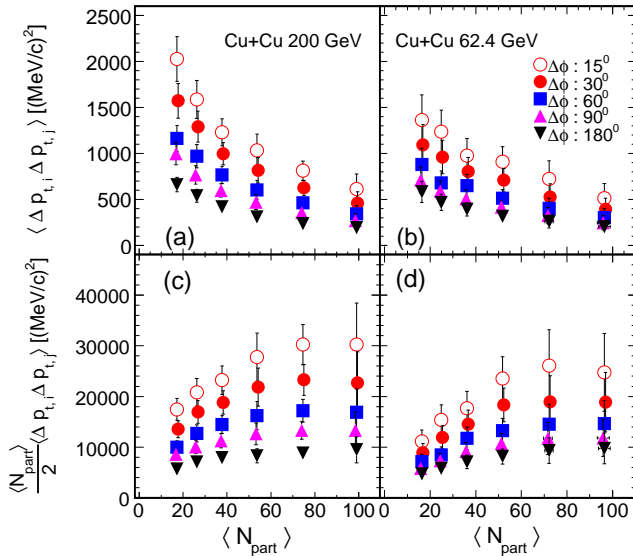


FIG. 6: (Color online) p_t correlations for varying azimuthal acceptance for Cu+Cu collisions at $\sqrt{s_{NN}} = 200$ GeV [panels (a) and (c)] and 62.4 GeV [panels (b) and (d)].

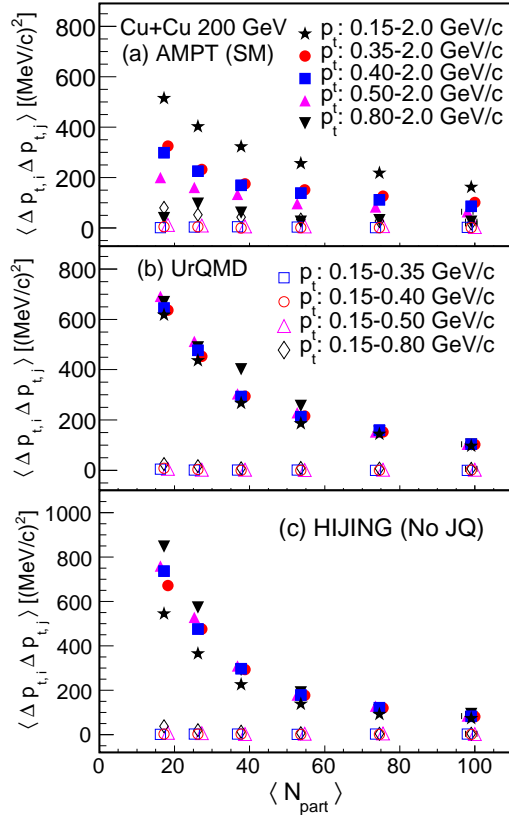


FIG. 8: (Color online) Correlations for varying p_t ranges for different model calculations in Cu+Cu 200 GeV: (a) AMPT (SM), (b) URQMD, and (c) Hijing (no JQ).

show p_t correlations that are similar to those observed in data for corresponding variations in the p_t windows. The trend of the correlation values shown by both URQMD and HIJING is similar to what is seen in the data for the low- p_t windows where the lower bound is fixed at 0.15 GeV/ c and the upper bound is increased from 0.35 GeV/ c to 0.50 GeV/ c . However, for URQMD, if the higher p_t bound is fixed at 2.0 GeV/ c and the lower p_t bound is subsequently decreased to 0.15 GeV/ c , p_t correlation values remain similar. For the same case, HIJING shows a decrease in p_t correlation values when the lower p_t bound is decreased to 0.15 GeV/ c . This is just the opposite of what is observed in data as seen in Fig. 7.

Because correlations are calculated for different p_t ranges, the p_t acceptance effect on the observed p_t correlations, is examined. The correlation values in different p_t ranges may depend on the p_t range size and on the fluctuations in the p_t spectrum slope in that p_t range. It is, therefore, important to see the effect of slope fluctuations on the correlation values in different p_t ranges. The p_t correlations can be formulated in terms of the fluctuations in the inverse slope parameter (effective tempera-

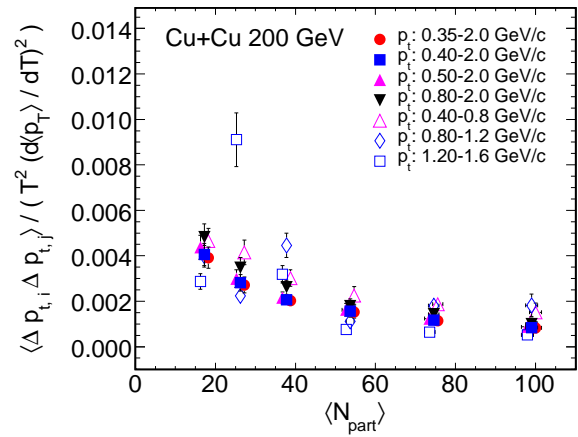
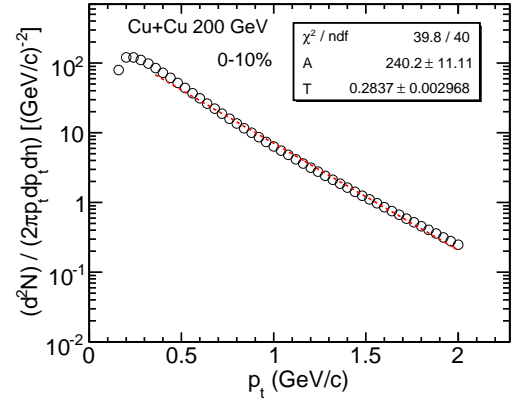


FIG. 9: (Color online) Top panel: Uncorrected inclusive charged particle p_t spectrum for 0%–10% collision centrality for Cu+Cu 200 GeV (open circles). The distribution is a fit to the exponential function: $Ae^{-p_t/T}$ (red dashed line). Errors are statistical. Bottom panel: Correlations scaled by $(d\langle p_t \rangle / dT)^2 T^2$ vs. $\langle N_{\text{part}} \rangle$ for different p_t ranges in Cu+Cu 200 GeV.

ture) by the following relation [17]:

$$\langle \Delta p_t \Delta p_t \rangle \approx \left[\frac{d\langle p_t \rangle}{dT} \right]^2 \Delta T^2, \quad (7)$$

where ΔT^2 describes the fluctuation in the inverse slope parameter. The dependence $\langle p_t(T) \rangle$ can be obtained from the function that describes the inclusive uncorrected p_t spectrum for the desired p_t range in the following manner. Figure 9 (top panel) shows the measured inclusive p_t spectrum for 0%–10% collision centrality in Cu+Cu collisions at 200 GeV. The dashed line represents the exponential fit of the form $F(p_t) = Ae^{-p_t/T}$ that is fit to these measurements for the p_t range 0.35–2.0 GeV/ c . The expressions for $\langle p_t \rangle$ and $(d\langle p_t \rangle / dT)$ can be obtained

using the following relation:

$$\langle p_t \rangle = \frac{\int_a^b p_t^2 F(p_t) dp_t}{\int_a^b p_t F(p_t) dp_t}, \quad (8)$$

which gives,

$$\langle p_t \rangle = 2T + \frac{a^2 e^{-a/T} - b^2 e^{-b/T}}{(a+T)e^{-a/T} - (b+T)e^{-b/T}}. \quad (9)$$

Here, a and b are the lower and upper limits of a given p_t range, respectively. The derivative of $\langle p_t \rangle$ with respect to T is obtained as:

$$\frac{d\langle p_t \rangle}{dT} = 2 - \frac{Ae^{-(a+b)/T} + a^2 e^{-2a/T} + b^2 e^{-2b/T}}{[(a+T)e^{-a/T} - (b+T)e^{-b/T}]^2}, \quad (10)$$

where

$$A = \frac{ab(b-a)^2}{T^2} + \frac{(b^2 - a^2)(b-a)}{T} - (a^2 + b^2). \quad (11)$$

Using the lower and upper limits of a given p_t range, and the corresponding T from the spectrum fit for each p_t range and collision centrality, $(d\langle p_t \rangle/dT)^2 T^2$ are obtained for every p_t range in each centrality.

Figure 9 (bottom panel) shows the measured two-particle p_t correlations scaled by $(d\langle p_t \rangle/dT)^2 T^2$ vs. $\langle N_{\text{part}} \rangle$ for different p_t ranges in Cu+Cu 200 GeV. The data points for p_t ranges (in GeV/c): 0.4–0.8, 0.5–2.0, 1.2–1.6, and 0.35–2.0, are shifted by one unit in $\langle N_{\text{part}} \rangle$ for clarity. The scaled p_t correlations for different p_t ranges become similar and show little dependence on the collision centrality. This study seems to suggest that the difference in the p_t correlations for different p_t ranges may due to the fluctuations in slope of the p_t spectrum in those p_t ranges.

V. SYSTEMATIC UNCERTAINTIES

Systematic errors on the mean (μ) and standard deviation (σ) in the $\langle p_t \rangle$ distributions (discussed in Sec. III), and p_t correlations (discussed in Sec. IV) are mainly evaluated by varying the different cuts used in the analysis, re-doing the analysis using these changed cuts and determining the resulting changes in the values of μ , σ , and the p_t correlations. The difference is taken as the systematic error due to a particular analysis cut. The resulting systematic uncertainties, described below, are shown in Tables III and IV as a percentage of the result (μ , σ , and the p_t correlations) for various centralities for Cu+Cu collisions at both 62.4 and 200 GeV.

To study the effect of the z-vertex (V_z) cut, the V_z acceptance is increased to ± 50 cm from the default value of ± 30 cm. No change in μ or σ or in the p_t correlations is observed when using the wider V_z .

TABLE III: Systematic errors on μ and σ in event-wise $\langle p_t \rangle$ distributions as described in Sec. III for various collision centralities in Cu+Cu collisions at $\sqrt{s_{NN}} = 62.4$ and 200 GeV.

| % cross section | Cu+Cu 62.4 GeV | | | | Cu+Cu 200 GeV | | | |
|-----------------|----------------|--------------------------|------------------|-----------------------------|---------------|--------------------------|------------------|-----------------------------|
| | DCA μ (%) | $N_{\text{Fit}} \mu$ (%) | DCA σ (%) | $N_{\text{Fit}} \sigma$ (%) | DCA μ (%) | $N_{\text{Fit}} \mu$ (%) | DCA σ (%) | $N_{\text{Fit}} \sigma$ (%) |
| 0-10 | 3.6 | 0.4 | 7.9 | 1.0 | 3.4 | 0.24 | 5.7 | 1.2 |
| 10-20 | 3.6 | 0.4 | 7.1 | 1.0 | 3.3 | 0.23 | 5.2 | 1.2 |
| 20-30 | 3.6 | 0.4 | 6.6 | 1.0 | 3.3 | 0.23 | 5.2 | 1.1 |
| 30-40 | 3.6 | 0.4 | 6.2 | 1.0 | 3.3 | 0.20 | 4.7 | 1.2 |
| 40-50 | 3.6 | 0.4 | 6.0 | 1.0 | 3.2 | 0.20 | 4.9 | 1.1 |
| 50-60 | 3.6 | 0.4 | 6.0 | 1.0 | 3.2 | 0.22 | 4.4 | 1.2 |

TABLE IV: Systematic errors on p_t correlations as described in Sec. IV for various collision centralities in Cu+Cu collisions at $\sqrt{s_{NN}} = 62.4$ GeV and 200 GeV.

| % cross section | Cu+Cu 62.4 GeV | | | | Cu+Cu 200 GeV | | | |
|-----------------|----------------|----------------------|-----------|---------------|---------------|----------------------|-----------|---------------|
| | DCA (%) | N_{Fit} (%) | Poly. (%) | Low p_t (%) | DCA (%) | N_{Fit} (%) | Poly. (%) | Low p_t (%) |
| 0-10 | 30 | 1.4 | 1.9 | 7.2 | 16 | 0.05 | 1.9 | 22 |
| 10-20 | 23 | 0.8 | 3.6 | 13.1 | 13 | 0.09 | 3.6 | 3.2 |
| 20-30 | 18 | 0.6 | 1.9 | 3.4 | 13 | 1.1 | 1.9 | 12.3 |
| 30-40 | 17 | 1.0 | 0.004 | 9.0 | 8 | 1.2 | 0.004 | 9.7 |
| 40-50 | 19 | 3.0 | 0.009 | 1.0 | 10 | 2.0 | 0.009 | 8.4 |
| 50-60 | 20 | 3.6 | 0.009 | 4.0 | 7 | 5.0 | 0.009 | 8.3 |

The effect of the cuts used to suppress background tracks is studied by changing the DCA cut from the default, $\text{DCA} < 1$ cm, to $\text{DCA} < 1.5$ cm and separately, changing the required number of fit points along the track, N_{Fit} , from the default $N_{\text{Fit}} > 20$ to $N_{\text{Fit}} > 15$. The resulting systematic errors due to these changes are listed in Tables III and IV in the columns labeled “DCA” and “ N_{Fit} ”.

The effect of the size of the centrality bin on the p_t correlations is addressed by fitting $\langle \langle p_t \rangle \rangle$ as a function of $\langle N_{\text{ch}} \rangle$ (see Sec. IV). To determine the systematic uncertainty associated with this process, different polynomial functions are used to fit $\langle \langle p_t \rangle \rangle$ vs. $\langle N_{\text{ch}} \rangle$. The systematic errors associated with this correction are listed in Table IV in the columns labeled “Poly.”.

The systematic uncertainty on the p_t correlations that may be associated with the application of the low- p_t cut is estimated by removing this p_t cut in the HIJING [41] model calculations. The estimated systematic errors are shown in Table IV in the columns labeled “Low p_t ”.

The p_t correlations may also include short range correlations such as Coulomb interactions and Hanbury Brown-Twiss (HBT) correlations. These correlations usually dominate among pairs of particles having relative transverse momentum less than 100 MeV/c. The

effect of these short-range correlations on the measured p_t correlations is seen by calculating p_t correlations after removing the pairs of particles with relative momentum ($p_i - p_j$), less than 100 MeV/ c . The p_t correlations are reduced by a maximum of 6% when short-range correlations are excluded.

The p_t correlations also include the contributions from resonance decays and charge ordering. These correlations are obtained for pairs of particles having like ($++$ or $--$) and unlike ($+-$) charges with respect to inclusive charged particles. A maximum of 15% decrease in the correlations is observed for pairs of particles with like charges and about 12% increase is observed for pairs with unlike charges with respect to the correlations for inclusive charged particle pairs for Cu+Cu collisions at $\sqrt{s_{NN}} = 62.4$ GeV and 200 GeV.

VI. SUMMARY

We have reported measurements of p_t fluctuations in Cu+Cu collisions in the STAR detector at RHIC for $\sqrt{s_{NN}} = 62.4$ and 200 GeV, and compared with Au+Au collisions at the same energies to investigate the system size dependence. The dynamical p_t fluctuations are observed by comparing data to mixed events in both Cu+Cu and Au+Au collisions at these two beam energies. Moreover, for similar mean number of participating nucleons, the p_t fluctuations are observed to be comparable for the Cu+Cu and Au+Au systems, suggesting that the system size has little effect. In addition, p_t correlation measurements for Cu+Cu collisions at $\sqrt{s_{NN}} = 62.4$ and 200 GeV are compared with the published Au+Au measurements. For both Cu+Cu and Au+Au systems, the p_t correlation decreases with increasing $\langle N_{\text{part}} \rangle$ at both beam energies. The dilution of the p_t correlations with increasing $\langle N_{\text{part}} \rangle$ could be due to the decrease in correlations that are dominated by pairs of particles that originate from the same nucleon-nucleon collision. A similar observation is found with other fluctuation and correlation observables such as K/π [37] and net charge [43].

The p_t correlations are found to scale with number of participating nucleon pairs for $\langle N_{\text{part}} \rangle > 100$ (when the system size is larger than that of central Cu+Cu collisions). This might indicate the onset of thermalization [26], the onset of jet quenching [3, 11], or the saturation of transverse flow in central collisions [38]. The square root of the p_t correlations normalized by eventwise average transverse momentum for Cu+Cu and Au+Au collisions is similar for systems with similar $\langle N_{\text{part}} \rangle$ and is independent of the beam energies studied.

The results described above are compared to predictions from several relevant model calculations. The transport-based URQMD model calculations are found to have a better quantitative agreement with the measurements compared to models which incorporate only

jet-like correlations as in HIJING. HIJING gives similar dependence on $\langle N_{\text{part}} \rangle$, but under predicts the magnitude. Inclusion of the jet-quenching effect in HIJING leads to a smaller value of the correlations in central collisions. A multiphase transport model calculation incorporating coalescence as a mechanism of particle production also compares well with data for central collisions.

When studying the p_t correlations for different p_t intervals, the correlations appear to be small and fairly independent of p_t interval, if the lower p_t bound is fixed at 0.15 GeV/ c and the higher p_t bound is progressively increased up to 0.50 GeV/ c . This suggests that correlations are weak for low- p_t particles. This low- p_t trend observed in the data is also seen in URQMD, AMPT, and HIJING models. When the analysis is carried out keeping the higher p_t bound fixed at 2.0 GeV/ c and progressively decreasing the lower p_t bound to $p_t = 0.15$ GeV/ c , the correlation values in data are found to increase. This suggests that high p_t particles are more correlated with low- p_t particles. The AMPT model shows a rather similar variation of p_t correlations for different p_t intervals, as observed in data. The URQMD model calculations, however, show no such variations in correlations for the different p_t intervals with higher p_t bound fixed at 2.0 GeV/ c . Finally, it is noted that the HIJING model calculations give p_t correlations that decrease with a decrease in the lower p_t bound for intervals with fixed higher p_t ($= 2.0$ GeV/ c) bound, i.e., opposite to what is observed in data. Regarding the changes in p_t correlations in different p_t intervals, it is found that the resultant fluctuations after considering event-by-event variation in the slope of the p_t spectra for different p_t bins are all of similar order.

The variation of p_t correlation with the change in the accepted range of pseudorapidity and azimuthal angle of the produced particles, are also shown. The correlation values increase when the η - and the ϕ -acceptance are reduced.

VII. ACKNOWLEDGEMENTS

We thank the RHIC Operations Group and RCF at BNL, the NERSC Center at LBNL and the Open Science Grid consortium for providing resources and support. This work was supported in part by the Offices of NP and HEP within the U.S. DOE Office of Science, the U.S. NSF, the Sloan Foundation, CNRS/IN2P3, FAPESP CNPq of Brazil, Ministry of Education and Science of the Russian Federation, NNSFC, CAS, MoST, and MoE of China, GA and MSMT of the Czech Republic, FOM and NWO of the Netherlands, DAE, DST, and CSIR of India, the Polish Ministry of Science and Higher Education, the National Research Foundation (NRF-2012004024), the Ministry of Science, Education and Sports of the Republic of Croatia, and RosAtom of Russia.

-
- [1] H. Heiselberg, Phys. Rep. **351**, 161 (2001).
- [2] H. Appelshauser *et al.* (NA49 Collaboration), Phys. Lett. B **459**, 679 (1999); D. Adamova *et al.* (CERES Collaboration), Nucl. Phys. A **727**, 97 (2003); K. Adcox *et al.* (PHENIX Collaboration), Phys. Rev. Lett. **89**, 212301 (2002).
- [3] S. S. Adler *et al.* (PHENIX Collaboration), Phys. Rev. Lett. **93**, 092301 (2004).
- [4] J. Adams *et al.* (STAR Collaboration), Phys. Rev. C **71**, 064906 (2005).
- [5] M. M. Aggarwal *et al.* (WA98 Collaboration), Phys. Rev. C **65**, 054912 (2002).
- [6] K. Adcox *et al.* (PHENIX Collaboration), Phys. Rev. C **66**, 024901 (2002).
- [7] J. Adams *et al.*, (STAR Collaboration), J. Phys. G **34**, 451 (2007); J. Phys. G **32**, L37 (2006).
- [8] M. Stephanov, K. Rajagopal and E. Shuryak, Phys. Rev. Lett. **81**, 4816 (1998).
- [9] M. Stephanov, K. Rajagopal and E. Shuryak, Phys. Rev. D **60**, 114028 (1999).
- [10] M. Stephanov, Phys. Rev. D **65**, 096008 (2002).
- [11] Q. Liu and T. A. Trainor, Phys. Lett. B **567**, 184 (2003).
- [12] J. D. Bjorken and E. A. Paschos, Phys. Rev. **185**, 1975 (1969).
- [13] L. Stodolsky, Phys. Rev. Lett. **75**, 1044 (1995).
- [14] S. Mrowczynski, Phys. Lett. B **430**, 9 (1998).
- [15] K. Rajagopal, hep-ph/9808348.
- [16] B. Berdnikov and K. Rajagopal, Phys. Rev. D. **61**, 105017 (2000);
- [17] S. A. Voloshin, V. Koch and H. G. Ritter, Phys. Rev. C **60**, 024901 (1999).
- [18] S. A. Bass, M. Gyulassy, H. Stöcker and W. Greiner, J. Phys. G **25**, R1 (1999).
- [19] S. A. Bass, P. Danielewicz and S. Pratt, Phys. Rev. Lett. **85**, 2689 (2000).
- [20] S. Jeon and V. Koch, Phys. Rev. Lett. **85**, 2076 (2000).
- [21] M. Asakawa, U. Heinz and B. Müller, Phys. Rev. Lett. **85**, 2072 (2000).
- [22] Z.-W. Lin and C. M. Ko, Phys. Rev. C **64**, 041901(R) (2001).
- [23] H. Heiselberg and A. D. Jackson, Phys. Rev. C **63**, 064904 (2001).
- [24] E. V. Shuryak and M. A. Stephanov, Phys. Rev. C **63**, 064903 (2001).
- [25] C. Pruneau, S. Gavin and S. Voloshin, Phys. Rev. C **66**, 044904 (2002).
- [26] S. Gavin, Phys. Rev. Lett. **92**, 162301 (2004).
- [27] M. Rybczynski *et al.* (for NA49 Collaboration), J. Phys. G **35**, 104091 (2008).
- [28] T. Anticic *et al.* (NA49 Collaboration), Phys. Rev. C **79**, 044904 (2009); K. Grebieszko (for the NA49 and NA61 Collaborations), Acta Phys. Polon. B **41**, 427 (2010).
- [29] B. I. Abelev *et al.* (STAR Collaboration), Phys. Rev. C **81**, 024911 (2010); STAR Internal Note-SN0493, 2009; arXiv:1007.2613; L. Kumar (STAR Collaboration), Nucl. Phys. A **830**, 275C (2009); L. Kumar (STAR Collaboration) *ibid.* **862**, 125 (2011); B. Mohanty *ibid.* **830**, 899C (2009).
- [30] J. Adams *et al.* (STAR Collaboration), Phys. Rev. C **72**, 044902 (2005).
- [31] F. S. Bieser *et al.*, Nucl. Instr. Meth. A **499**, 766 (2003).
- [32] K. H. Ackermann *et al.* (STAR Collaboration), Nucl. Instr. Meth. A **499**, 624 (2003).
- [33] H. Bichsel, Nucl. Instr. Meth. A **562**, 154 (2006).
- [34] B. I. Abelev *et al.* (STAR Collaboration), Phys. Rev. C **79**, 034909 (2009); R. L. Ray and M. S. Daugherty, J. Phys. G: Nucl. Part. Phys. **35**, 125106 (2008); D. Kharzeev and M. Nardi, Phys. Lett. B **507**, 121 (2001); A. Timmins, Ph. D. Thesis, University of Birmingham, 2008 (unpublished).
- [35] M. J. Tannenbaum, Phys. Lett. B **498**, 29 (2001).
- [36] S. V. Afanasiev *et al.* (NA49 Collaboration), Phys. Rev. Lett. **86**, 1965 (2001).
- [37] B. I. Abelev *et al.* (STAR Collaboration), Phys. Rev. Lett. **103**, 092301 (2009).
- [38] S. A. Voloshin, Phys. Lett. B **632**, 490 (2006).
- [39] S. A. Bass *et al.*, Prog. Part. Nucl. Phys. **41**, 255 (1998); M. Bleicher *et al.*, J. Phys. G **25**, 1859 (1999).
- [40] Z.-W. Lin and C. M. Ko, Phys. Rev. C **65**, 034904 (2002); Z.-W. Lin, C. M. Ko, B. A. Li, B. Zhang, and S. Pal, *ibid.* **72**, 064901 (2005); L.-W. Chen *et al.*, Phys. Lett. B **605**, 95 (2005).
- [41] X. N. Wang and M. Gyulassy, Phys. Rev. D **44**, 3501 (1991).
- [42] B. Andersson, G. Gustafson, G. Ingelman, and T. Sjöstrand, Phys. Rep. **97**, 31 (1983).
- [43] B. I. Abelev *et al.* (STAR Collaboration), Phys. Rev. C **79**, 024906 (2009).